Applied Thermal Engineering 258 (2025) 124536

Contents lists available at ScienceDirect

Applied Thermal Engineering

journal homepage: www.elsevier.com/locate/ate

Research Paper

# Quantifying the effects of spectral and directional distribution of radiation on its propagation in saline water

Nan Deng [a], Peixin Dong [a], Zhe Wang [b,c,1], Mengying Li [a,*,1]

[a] Department of Mechanical Engineering & Research Institute for Smart Energy, The Hong Kong Polytechnic University, Hong Kong Special Administrative Region of China

[b] Department of Civil and Environmental Engineering, The Hong Kong University of Science and Technology, Hong Kong Special Administrative Region of China

[c] HKUST Shenzhen-Hong Kong Collaborative Innovation Research Institute, Futian, Shenzhen, China

ARTICLE INFO

*Keywords:*
Radiative transfer in water
Spectral and directional radiation
Monte Carlo method
Solar evaporation
Energy-related applications

ABSTRACT

The interactions of radiation with saline water facilitate various energy-related applications, such as radiative evaporation at the air–water interface, radiation-driven underwater vapor generation, and underwater photovoltaic systems. However, these applications require a comprehensive understanding of radiation propagation through saline water, considering both its spectral and directional characteristics, which are often inadequately explored. This study introduces a three-dimensional Monte Carlo radiative transfer model equipped with fine spectral resolution and detailed angular considerations. The model simulates the transfer of radiation from the air to the air–water interface and throughout the saline water body to thoroughly examine the effects of spectral and directional properties of incident radiation on its propagation across different depths of saline water. The findings reveal that within the solar spectrum, radiation entering the water at a 62.7-degree angle of incidence and completely diffuse radiation exhibit similar absorption effects in water layers less than 2 meters deep. In addition, the incident angle has little impact on the absorption rate of both the water surface and the water body when the angle is below 62.7°. Spectrally, radiation wavelengths longer than 1.4 μm, 1.14 μm, and 1 μm are fully absorbed within the first 1, 8, and 50 centimeters of saline water, respectively, representing approximately 20%, 30%, and 50% of incident solar radiation. Additionally, radiation from blackbody sources below 1300 Kelvin is absorbed entirely within the top 1 centimeter of saline water. Empirical correlations are then developed to easily estimate the absorption rate based on the depth of the water and the temperature of the blackbody heat source. The findings elucidate the influence of the spectral and directional characteristics of incident radiation on its underwater propagation, offering essential guidance for the design and performance evaluation of various energy-centric applications.

## 1. Introduction

Radiative transfer, which encompasses the absorption, emission, and scattering processes, is a key factor in the analysis of atmospheric and oceanic circulation, which also significantly influences climate patterns [1]. Radiative transfer processes are also vital for various energy applications. For example, solar radiation transmitted through the atmosphere drives solar energy systems, while solar radiation transmitted in shallow water (<2 m) supports technologies such as radiative evaporation, seawater desalination [2–7], contamination discharge [8], steam sterilization [9], and underwater photovoltaic (PV) [10,11]. These technologies have underscored the importance of understanding how radiation interacts with air, pure water, and saline water. Considering that more than 97% of Earth's water is seawater and many energy applications are likely to be deployed in saline environments, comprehending the interactions between radiation and saline water is particularly crucial [2].

Interfacial evaporation applications utilize spectrally selective absorbers to localize incident radiation on the water surface [8]. These absorbers either conduct heat (contact evaporation) or emit longwave radiation on the surface of the water (contactless evaporation), facilitating the direct utilization of heat for evaporation [12,13]. Some applications employ PV panels as absorbers to maximize the full use of the solar spectrum [10,14,15]. The interfacial evaporation efficiency is significantly influenced by the radiation spectrum emitted by these absorbers and the corresponding quantity received by the water surface [2,8]. However, few studies have clearly quantified how

* Corresponding author.
*E-mail addresses:* cezhewang@ust.hk (Z. Wang), mengying.li@polyu.edu.hk (M. Li).

[1] The two authors have the same contribution to this study.

https://doi.org/10.1016/j.applthermaleng.2024.124536
Received 3 May 2024; Received in revised form 8 September 2024; Accepted 1 October 2024
Available online 9 October 2024
1359-4311/

## Nomenclature

### Variables

| | |
|---|---|
| $(r_x, r_y, r_z)$ | Direction vector of a photon |
| $(x, y, z)$ | Position of a photon in Cartesian coordinates, [cm] |
| $(x_e, y_e, z_e)$ | Coordinates of a side surface, [cm] |
| $d_b$ | Distance to the next boundary along the propagation path, [cm] |
| $d_c$ | Distance to next collision point, [cm] |
| $d_e$ | Distance to the nearest edge along the propagation path, [cm] |
| $e_\nu$ | Monochromatic energy carried by a single photon, [W/cm$^{-1}$] |
| $E_b$ | Total emissive power of a blackbody, [W/m$^2$] |
| $E_{b\nu}$ | Monochromatic blackbody emissive flux at wavenumber $\nu$, [W/(m$^2$ cm$^{-1}$)] |
| $G_\nu$ | Monochromatic solar irradiance at wavenumber $\nu$, [W/(m$^2$ cm$^{-1}$)] |
| $n_{\mathrm{w}}$ | Refractive index of water |
| $r_c$ | Convergence rate |
| $T$ | Temperature, [°C] |

### Constants

| | |
|---|---|
| $\kappa_B$ | Boltzmann constant, 1.3806485×10$^{-23}$ [J/K] |
| $\sigma$ | Stefan–Boltzmann constant, 5.67037×10$^{-8}$ [W/(m$^2$ K$^4$)] |
| $c$ | Speed of light, 2.99792458×10$^8$ [m/s] |
| $h$ | Planck constant, 6.62607015×10$^{-34}$ [J s] |
| $n_{\mathrm{air}}$ | Refractive index of air, 1.003 |

### Greek symbols

| | |
|---|---|
| $\alpha_\nu$ | Absorptivity of water at wavenumber $\nu$ |
| $\alpha_s$ | Absorptance of a surface |
| $\Delta\nu$ | Spectral resolution in terms of wavenumber, [cm$^{-1}$] |
| $\gamma_{\mathrm{az}}$ | Solar azimuth angle in the range of 0 to $2\pi$ |
| $\kappa_{\mathrm{abs}}$ | Absorption coefficient of water, [cm$^{-1}$] |
| $\kappa_{\mathrm{e}}$ | Extinction coefficient of water, [cm$^{-1}$] |
| $\kappa_{\mathrm{sca}}$ | Scattering coefficient of water, [cm$^{-1}$] |
| $\lambda$ | Wavelength, [μm] |
| $\mathcal{T}$ | Total transmission rate |
| $\mathcal{T}_\nu$ | Transmissivity of water body at wavenumber $\nu$ |
| $\mathcal{T}_s$ | Transmittance of a surface |
| $\nu$ | Wavenumber, [cm$^{-1}$] |
| $\rho_\nu$ | Single scattering albedo of water at wavenumber $\nu$ |
| $\rho_s$ | Reflectance of a surface |
| $\tau$ | Optical depth |
| $\Theta$ | Angle between incident direction and reflected/scattered direction |
| $\theta$ | Angle |
| $\theta_z$ | Solar zenith angle in the range of 0 to $\pi$ |
| α | Total absorption rate |
| ρ | Total reflection rate |
| $\zeta$ | Random number uniformly draw in the range of 0 to 1 |

### Subscripts

| | |
|---|---|
| $\nu$ | Wavenumber |
| ∥ | Parallel plane |
| ⊥ | Perpendicular plane |
| abs | Absorption |
| sca | Scattering |
| 0 | Initial status of variables |
| in | Incidence |
| tr | Transmission |
| b | Blackbody |

### Superscripts

| | |
|---|---|
| ′ | Updated status of variables |

### Abbreviations

| | |
|---|---|
| LBL | Line-By-Line |
| MAPE | Mean Absolute Percentage Error |
| MC-RTM | Monte Carlo Radiative Transfer Model |
| PV | Photovoltaic |
| RMSE | Root Mean Squared Error |
| RTM | Radiative Transfer Model |
| TOW | Top Of the Water |

the spectral characteristics of radiation emitted by the absorber affect its absorption by the water body. In the underwater environment, applications such as spectrally selective nanoparticles for steam generation [16–20] and underwater PV systems [11,21–23] are highly dependent on the distribution of the solar radiation spectrum at various depths to optimize energy conversion efficiency. When optical concentrators are used underwater to enhance solar energy intensity, it is also crucial to quantify the directional distribution of radiation as it passes through water [24–26]. In sum, these applications require a comprehensive understanding of the interaction between water and radiation with various spectral and directional characteristics.

The theoretical foundation of radiative transfer in water is robust, and extensive research on the distribution of solar radiation in shallow water ponds is well documented in the literature [27–29]. Despite this, the effects of the spectral and directional properties of incident radiation, particularly non-solar sources, remain inadequately quantified. Initial studies on the impact of spectral and directional characteristics of incident radiation on water absorption in solar ponds employed band models, which were resolved using numerical fitting methods that relied heavily on various assumptions [27,30–32]. These studies emphasized analysis, and quantification was constrained by limited accuracy. Subsequent research has leveraged Monte Carlo radiative transfer solvers, including commercial ray tracing software and Monte Carlo codes, to analyze radiation effects in various applications. For example, commercial software such as OptisWorks [33,34] and ZEMAX OpticStudio [35] have been employed to assess the performance of concentrated solar devices under direct and diffuse radiation conditions. Monte Carlo RTM codes have been used to simulate radiation propagation in the upper ocean [36,37] and within a body of nanofluids [38]. These advanced solvers have significantly improved the reliability of optical simulations in radiation-driven applications.

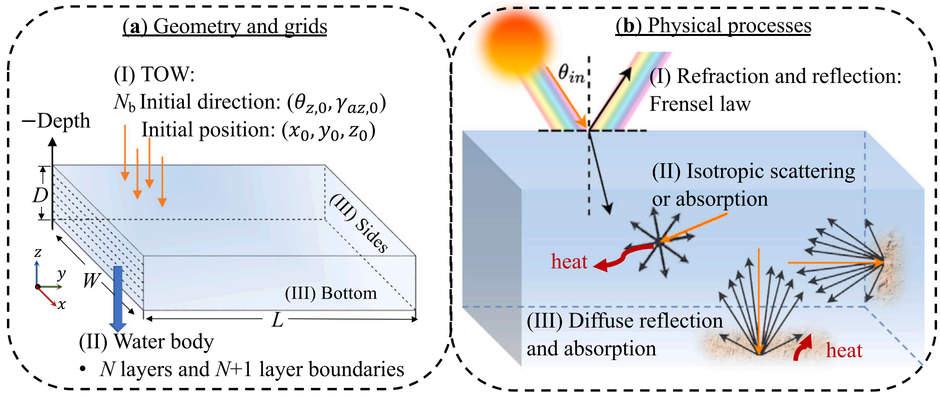


**Fig. 1.** Overview of the radiative transfer processes in a saline water pond. (a) Illustration of the geometry of the pond and the layout of the computational grid. (b) Physical processes that occur within the pond. The labeled processes (I, II, III) correspond to their respective positions (I, II, III) within the grid structure of the pond.

Although some studies have analyzed the spectral and directional impacts of radiation on water within a specific application environment [8,12,23], the findings are application-oriented and lack generalizability. For example, Menon et al. [8] and Wang et al. [39] demonstrated that converting solar radiation to the mid-infrared spectrum can significantly improve the efficiency of photothermal devices. Liang et al. [40] demonstrated the spectral splitting of solar radiation into two parts: sunlight near the band gap of the PV cell was used for electricity generation, while the remaining sunlight, at other wavelengths, was harnessed for thermal output. Wu et al. [41] proposed a solar spectral splitting and cascade utilization method and developed a thermodynamic model to evaluate the performance of the proposed system. Röhr et al. [23] examined how the solar spectrum varies at different depths of saline water to assess the efficiency of underwater photovoltaic systems [22,23]. Despite these advances, there remains a gap in existing studies that comprehensively consider the effects of both the angular and spectral characteristics of radiation during its interaction with water. Moreover, the majority of existing research focuses solely on solar radiation as the heat source, often overlooking the potential influences of radiation emitted by blackbodies (e.g. solar absorbers) at various temperatures. Consequently, it is essential to comprehensively quantify the effects of both the spectral and directional characteristics of incident radiation from various sources on its propagation through saline water, thereby providing more precise guidance for optimizing energy applications in related fields.

To address the identified research gaps, this study introduces a detailed Line-By-Line (LBL) Monte Carlo Radiative Transfer Model (MC-RTM) specifically designed to simulate the propagation of solar and blackbody emissive radiation in a saline water pond. This model allows for a comprehensive investigation on how the unique spectral and directional attributes of incident radiation influence its transport through saline water. Compared to commercial software such as Zemax, this Monte Carlo code offers high flexibility in modifying optical properties, handles complex geometries, ensures accurate simulations, adapts easily to various computational platforms, and is cost-effective. The insights derived from this research will offer essential guidance for the engineering and optimization of various energy systems, such as interfacial evaporation processes, subaqueous vapor generation technologies, and PV systems designed for underwater use. Specifically, the key contributions of this work are as follows:

- Development of a comprehensive radiative transfer model that retains the full complexity of spectral and angular dependence of radiation. This approach ensures that the model accurately reflects the true nature of radiation, without any spectral and angular simplification.
- Detailed quantification of how incident radiation is absorbed at varying depths of saline water. Three types of incident radiation are considered: direct solar (beam) radiation, scattered solar (diffuse) radiation, and blackbody (diffuse) emissive radiation. This comprehensive approach caters to the different ways in which radiation enters the water, accounting for its varied directional and spectral qualities.
- Derivation of straightforward empirical formulas that correlate the rate of radiation absorption to specific factors: the depth of the saline water and the temperature of the blackbody radiative source (or intensity of solar radiation). These correlations enable an easy prediction of radiation behavior based on key environmental parameters.

Section 2 details the algorithm of the MC-RTM model and its physical foundation. Based on the MC-RTM, Section 3 examines the interaction of radiation with water from the perspective of directionality and spectrum (and the heat source temperature). Finally, the findings and future outlook are summarized in Section 4.

## 2. Methodology

Section 2.1 presents a detailed description of the radiative transfer processes in the saline water pond, focusing on its model parameters and general physical processes. Section 2.2 introduces the evaluation of the optical properties of saline water and discusses the impacts of temperature and salinity on the optical properties. The characteristics of the incident radiation are presented in Section 2.3. The algorithms of MC-RTM in Section 2.4 include the simulation of absorption (Beer's law) and isotropic scattering, as well as diffuse reflection and reflection on the water surface (Fresnel law) [29].

### 2.1. Radiative transfer processes in water pond

As shown in Fig. 1a, the water pond consists of a Top Of the Water (TOW) interface, a water body, four sides, and one bottom surface. At the TOW, $N_b$ number of radiative energy carriers (i.e., photons) uniformly impinge on the entire surface of water. The water body is divided horizontally into multiple layers based on a resolution of $\Delta l$ [42]. Each water layer has an upper and a lower boundary where radiative flux through each layer will be evaluated. The bottom surface and the four sides of the pond are composed of soil. The physical processes at each location (I, II, III) are illustrated in Fig. 1b. (I) At the TOW, incident photons are either reflected off or refracted by the interface according to the Frensel law [29]. (II) Once entering the water body, photons are subject to absorption or isotropic scattering. (III) Interactions with the bottom surface or sides of the pond result in absorption or diffuse reflection of the photons.

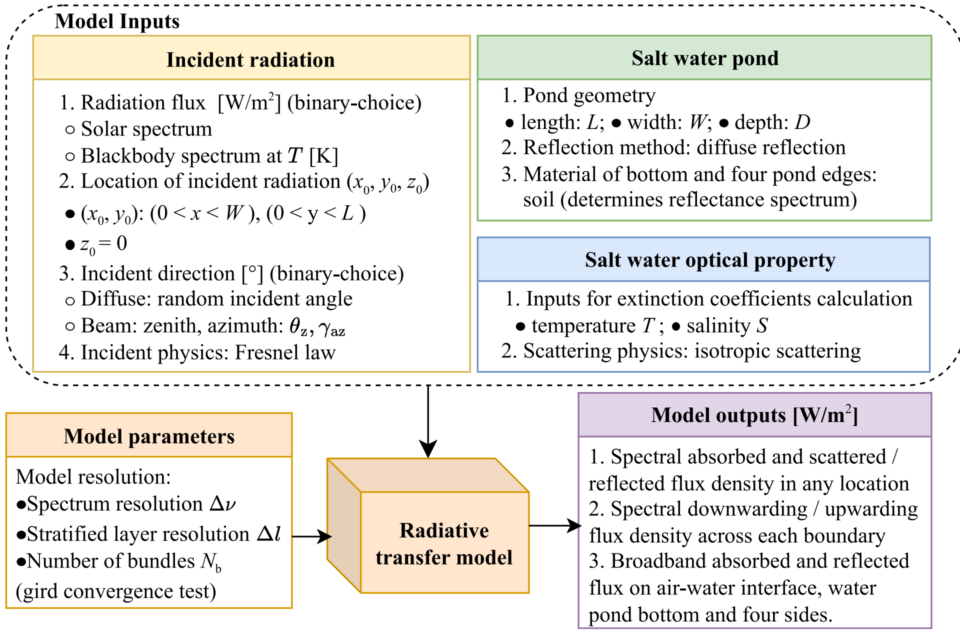


**Fig. 2.** Overview of the radiative transfer modeling process.

In the modeling process, the following presumptions are made: (i) The MC-RTM is constructed within a 3D Cartesian coordinate system. (ii) The system is considered to be in a steady state, disregarding fluid dynamics such as natural convection. (iii) The water surface is assumed to be plane-parallel and the saline water medium is considered homogeneous, with uniform temperature and salinity throughout. (iv) The reflections of light at the bottom surface and the sides of the water body are considered to be diffuse. (v) The scattering of light within the water is isotropic.

The boundary conditions for TOW, the four sides and the bottom of the pond are: (i) At the TOW, the initial grids and the zenith angle of the incident photons are as presented in Section 2.4.1. The energy carried by each photon is described in Section 2.3. (ii) The bottom and four sides have a constant reflectance of 0.01 for the visible band and 0.093 for all other spectral bands ($\lambda$ > 0.4 μm), as sourced from the ECOSTRESS spectral library [43,44]. Note that the TOW and the pond surfaces are considered as boundaries. Only reflection or transmission will occur at the TOW, whereas reflection or absorption will occur at the pond surfaces. The “water surface” in the following context is denoted as the top one centimeter of saline water, within which photons can be absorbed or scattered.

These radiative transfer processes are then simulated by the MC-RTM model (Section 2.4), with model inputs related to the saline water pond and incident radiation, as shown in Fig. 2. The modeling outputs are radiative flux at any location in the water pond.

The values of parameters related to the saline water pond are tabulated in Table 1. The dimensions of the pond are set at 20 × 20 meters in length and width, and depths varying from 0 to 2 m, which is the typical depth range of traditional evaporation ponds [8]. These dimensions ensure an aspect ratio greater than 10:1, which could effectively minimize the influence of pond edges [45]. These depths and water properties are selected to simulate scenarios relevant to contactless evaporation and seawater desalination [18,46]. The zenith angle of the incident photon, denoted $\theta_{z,0}$, is a variable that can be considered for incident radiation with different directional characteristics. Note that the incident azimuth angle is set to zero degree, considering that the optical properties are often azimuth-independent.

**Table 1**
Properties of the saline water pond.

| Name | Symbol | Value |
|---|---|---|
| Pond length | $L$ | 20 m |
| Pond width | $W$ | 20 m |
| Pond depth | $D$ | 0 to 2 m |
| Water temperature | $T$ | 20 °C |
| Water salinity | $S$ | 35 ppt |
| Photon initial zenith angle | $\theta_{z,0}$ | Variable |
| Photon initial azimuth angle | $\gamma_{az,0}$ | 0 |
| Photon initial position | $(x_0, y_0, z_0)$ | $(0 < x_0 < W,\ 0 < y_0 < L,\ 0)$ |
| Number of photon bundles at each wavenumber | $N_b$ | 1000 |
| The resolution of water stratified layers | $\Delta l$ | 1 cm |
| Spectral resolution | $\Delta \nu$ | 3 cm$^{-1}$ |
| Spectral reflectance of soil | $\rho_{s,\nu}$ | 0.01 ($\lambda \leq 0.4$); 0.093 ($\lambda > 0.4$) |

### 2.2. Optical properties of water

This section first presents methods for calculating the absorption and scattering coefficients of saline water. Then, how temperature (0–40 °C) and salinity (0–360 ppt) affect the scattering and absorption coefficients are investigated.

The index of refraction of water in Fig. 3a determines the reflection of radiation at the air–water interface via the Fresnel law. Additionally, the real and imaginary parts of the index of refraction determine the scattering and absorption of light in a water body, respectively. Both the absorption and scattering coefficients are influenced by factors such as temperature and salinity. The empirical equations from Röttgers et al. [47] are used to calculate the absorption coefficients, whereas the scattering coefficients are derived by integrating the volume scattering function across all directions, as detailed in studies [29,48]. According to the analysis by Mobley [29], water with lower salinity and higher temperatures typically exhibits higher absorption coefficients and lower scattering coefficients.

Fig. 3b displays the range of the absorption and scattering coefficients of water with salinity of 0 to 360 ppt and temperature of 0 to 40 °C, while the solid line represents values at a fixed temperature (20 °C) and salinity (35 ppt). Generally, absorption is more prevalent than scattering for photons with wavelengths ranging from 0.45 to 4

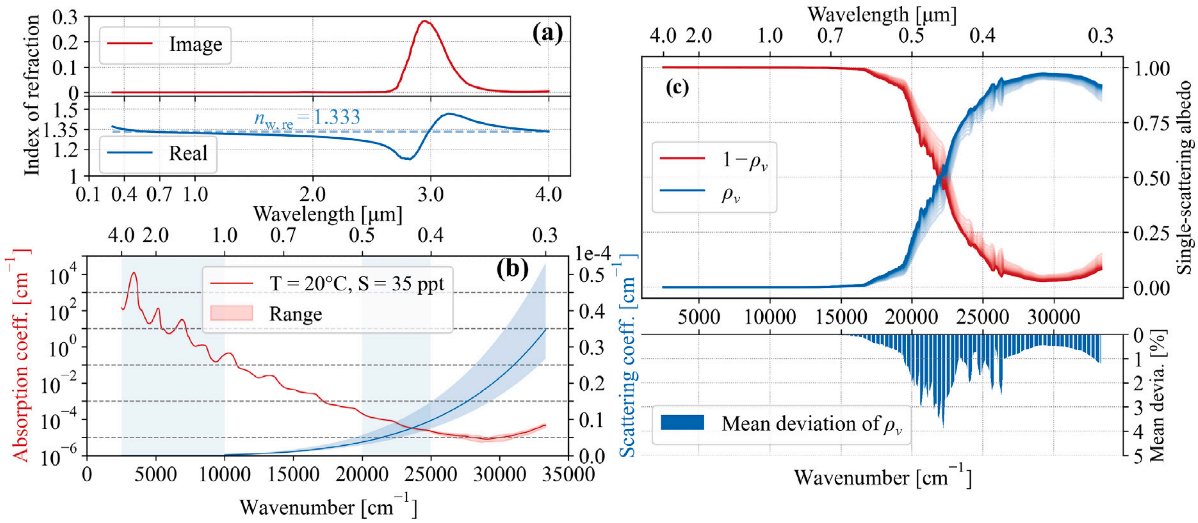


**Fig. 3.** Spectral optical properties of salt water of a wide range of temperature (0–40 °C) and salinity (0–360 ppt). (a) Index of refraction of water; (b) Absorption and scattering coefficients; (c) Single-scattering albedo and deviations due to the range of temperature and salinity.

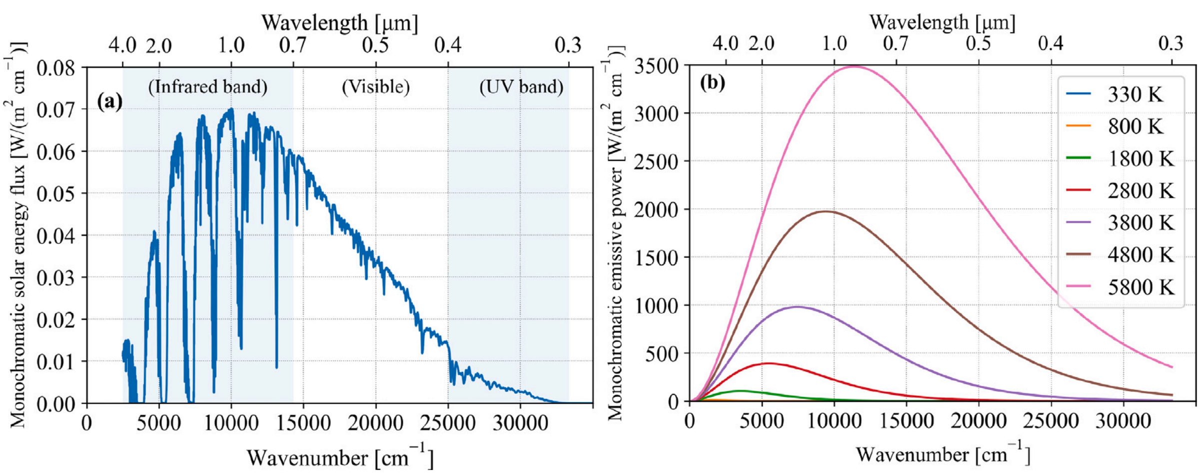


**Fig. 4.** (a) AM1.5 direct and circumsolar solar spectrum. (b) The monochromatic emissive power of a blackbody with various surface temperature.

μm, whereas photons with wavelengths shorter than 0.45 μm are more prone to scattering.

In the Monte Carlo simulation, the absorption and scattering processes in saline water are predominantly governed by the single scattering albedo ($\rho_v$) of the water particles, as shown in Fig. 3c (see Section 2.4.3 for details). Compared to fixed temperature and salinity, the deviation of the single scattering albedo is zero for the infrared band ($\lambda$ > 0.7 μm) and is less than 4% for the visible and UV bands ($\lambda$ < 0.7 μm). Given this small deviation, the optical properties of water in this work are set to those at a constant temperature of 20 °C and a salinity level of 35 ppt.

### 2.3. Spectral and directional characteristics of incident radiation

In this study, two distinct categories of incident radiation are examined, each characterized by its unique spectral distribution profile, as illustrated in Fig. 4. The first category encompasses solar radiation, which adheres to the standard AM1.5 direct and circumsolar spectrum and spans the wavelength range of 0.1 to 4 μm [49]. The second category pertains to blackbody radiation, which is evaluated across an extensive wavelength spectrum ranging from 0.1 to 200 μm, following Planck's law for spectral distribution [50,51],

$$E_{b,v}(T) = \frac{2\pi h c^2 v^3}{(e^{hcv/\kappa_B T} - 1)}, \tag{1}$$

where $T$ [K] is the heat source temperature, $h$ [J s] is the Planck constant, $c$ [m/s] is the speed of light, $\kappa_B$ [J/K] is the Boltzmann constant, and $v$ [cm$^{-1}$] is the wavenumber.

Directional distribution-wise, the incident radiation rays are either parallel with the same zenith angle (representing the solar beam) or diffuse with various zenith angles (for diffuse solar and blackbody heat sources). The incident photon then undergoes reflection and refraction at the air–water interface, altering its traveling direction. The angle of refraction adheres to Snell law,

$$n_{\text{air}} \sin\theta_{\text{in}} = n_{\text{w},v} \sin\theta_{\text{tr},v}, \tag{2}$$

where $n_{\text{air}}$ is the refractive index of air, which is set to 1.003, and $n_{\text{w},v}$ is the refractive index of water, which varies with wavelength (as shown in Fig. 3a) [29]. $\theta_{\text{in}}$ is the angle of incidence (which is equal to the zenith angle for a horizontal surface), and $\theta_{\text{tr},v}$ is the wavenumber-dependent refraction angle. The spectral reflectance of the air–water interface $\rho_{s,v}$ follows the Fresnel law,

$$\rho_{s,v}(\theta_{\text{in}}) = \frac{1}{2}\left\{\left[\frac{\sin(\theta_{\text{in}} - \theta_{\text{tr},v})}{\sin(\theta_{\text{in}} + \theta_{\text{tr},v})}\right]^2 + \left[\frac{\tan(\theta_{\text{in}} - \theta_{\text{tr},v})}{\tan(\theta_{\text{in}} + \theta_{\text{tr},v})}\right]^2\right\}. \tag{3}$$

In Fig. 5, the modeled reflectance at the air–water interface is depicted as a function of both wavelength and angle of incidence.

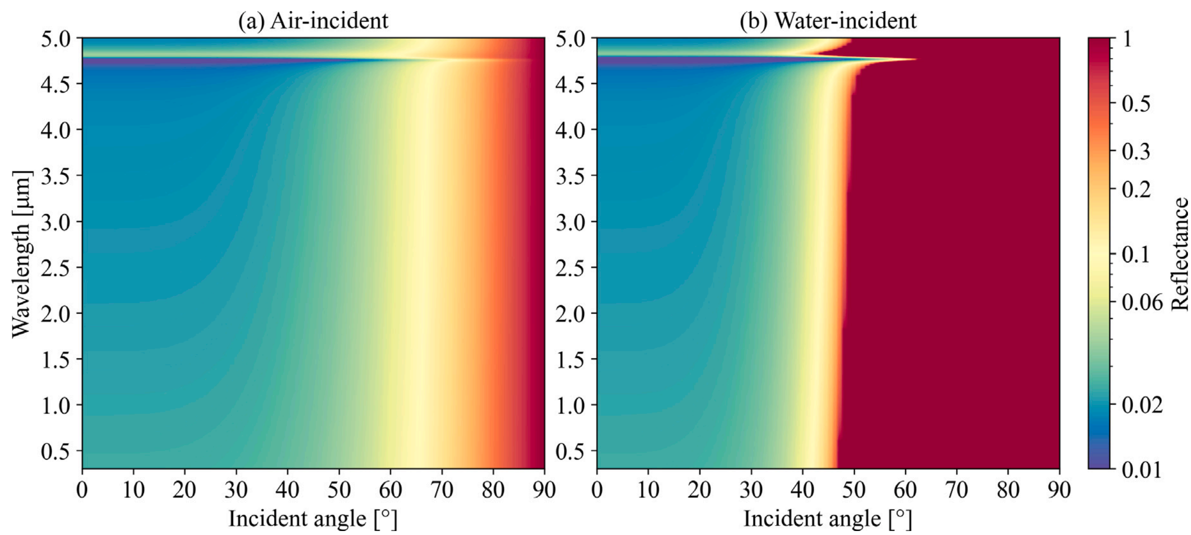


**Fig. 5.** Spectral reflectance with respect to angle of incidence for (a) incident radiation from air-to-water and (b) incident radiation from water-to-air.

When radiation approaches from the air side, the interface reflectance remains at less than 0.1 until the angle of incidence increases to 60 degrees. However, as the angle of incidence surpasses 70 degrees, the influx of photons entering the water body decreases substantially due to strong reflection. In contrast, for photons traveling from water to air, the reflectance of the interface is near unity beyond the critical angle of 46 degrees, as defined by Mobley [29], delineating the limit above which total reflection occurs. All these modeled results are consistent with well-established optical theories [29].

### 2.4. The Monte Carlo radiative transfer model

An LBL radiative transfer model based on the Monte Carlo method is developed to simulate how each photon propagates in saline water bodies. The model can be easily generalized to simulate radiative transfer in various media, including nanofluid, the atmosphere [52], and soil [53]. As a technique to trace each photon instead of solving the radiative transfer equations, the Monte Carlo method is based on a rigorous definition of the traveling probability of photons based on inherent optical properties and is more flexible and intuitive than other numerical analytical solutions [29]. It can be applied to any geometric configuration, which is particularly advantageous when additional objects make the geometry more complicated [29]. Recent advances in computational technology have made the Monte Carlo method more feasible for addressing complex problems [52]. The MC-RTM in this paper is an adaptation of the atmospheric MC-RTM developed by Li et al. [52]. The effects of polarization are not considered, as multipath scattering diminishes polarization in shallow water [54]. Furthermore, polarization mainly affects the directionality of the radiation rather than its quantity [29]. In the subsequent section, the principal elements of the aquatic MC-RTM are briefly described, with more details available in the work of Li et al. [52]. The MC-RTM generates output that includes the spectral and directional radiative intensity at various locations within the saline water pond, as well as the spectrum of radiative energy absorption in different horizontal water layers. Results from model convergence tests and the verification process are detailed in the Appendix.

#### 2.4.1. Photon initiation

After setting model inputs (Table 1) at each wavenumber, photons start their journey as depicted in the algorithm flowchart in Fig. 6. Each photon's initial position in the Cartesian coordinate system is assigned as $(x_0, y_0, z_0)$, uniformly distributed within the pond's surface area, with predefined zenith angle $\theta_z$ and azimuth angle $\gamma_{az}$ (Section 2.3). Each photon's initial direction vectors $(r_x, r_y, r_z)$ are defined as:

$$r_x = \sin\theta_z \cos\gamma_{az},\ \ r_y = \sin\theta_z \sin\gamma_{az},\ \ r_z = -\cos\theta_z. \tag{4}$$

In the LBL calculation mode, the monochromatic energy $e_\nu$ carried by each photon for solar and blackbody heat sources is:

$$\begin{aligned} e_\nu &= \frac{G_\nu \cdot L \cdot W}{N_b}, \\ e_\nu &= \frac{E_{b,\nu} \cdot L \cdot W}{N_b}, \end{aligned} \tag{5}$$

in which $L \cdot W$ is the surface area of the water pond. The $G_\nu$ and $E_{b,\nu}$ are monochromatic solar irradiance and blackbody irradiance at wavenumber $\nu$ in unit of [W/(m$^2$ cm$^{-1}$)], respectively.

Each photon undergoes a series of transport and collision events until all photons are either absorbed by the medium or exit the water pond through the air–water interface. The total number of photons traversing each boundary and those absorbed within each layer are recorded. This data is then used to multiply the energy carried by each photon, which in turn enables the calculation of the total energy reflected and absorbed by the water pond.

#### 2.4.2. Photon transport

After entering the water body, the traveling distance of a photon before its next collision with water particles is denoted as $d_c$. The distances to the next boundary and the pond sides along its path are $d_b$ and $d_e$, respectively, as defined in [52]:

$$\begin{aligned} d_c &= -\frac{\ln\zeta}{\kappa_e}, \\ d_b &= \frac{z_b - z}{r_z}, \\ d_e &= \min\left(\left|\frac{x_e - x}{r_x}\right|, \left|\frac{y_e - y}{r_y}\right|\right), \end{aligned} \tag{6}$$

where $\zeta$ is a uniformly generated random number between 0 and 1; $z_b$ is the $z$-coordinate of the next boundary; $x_e$ and $y_e$ are the coordinates of a side surface. The photons will travel layer by layer, resulting in three potential collision scenarios before they reach $d_c$, as illustrated in Fig. 6: (i) reflection or refraction on the air–water interface; (ii) collision with a side surface if $d_e = \min(d_c,\ d_b,\ d_e)$; (iii) collision within the current layer if $d_b < d_c$. If none of these occurs, (iv) the photon advances to the layer boundary. At boundaries other than the bottom surface or TOW, the photon's coordinate updates to $d_c'$ (as derived in [52]) and undergoes another round of (i–iv). These parameters $d_b'$, $d_e'$,

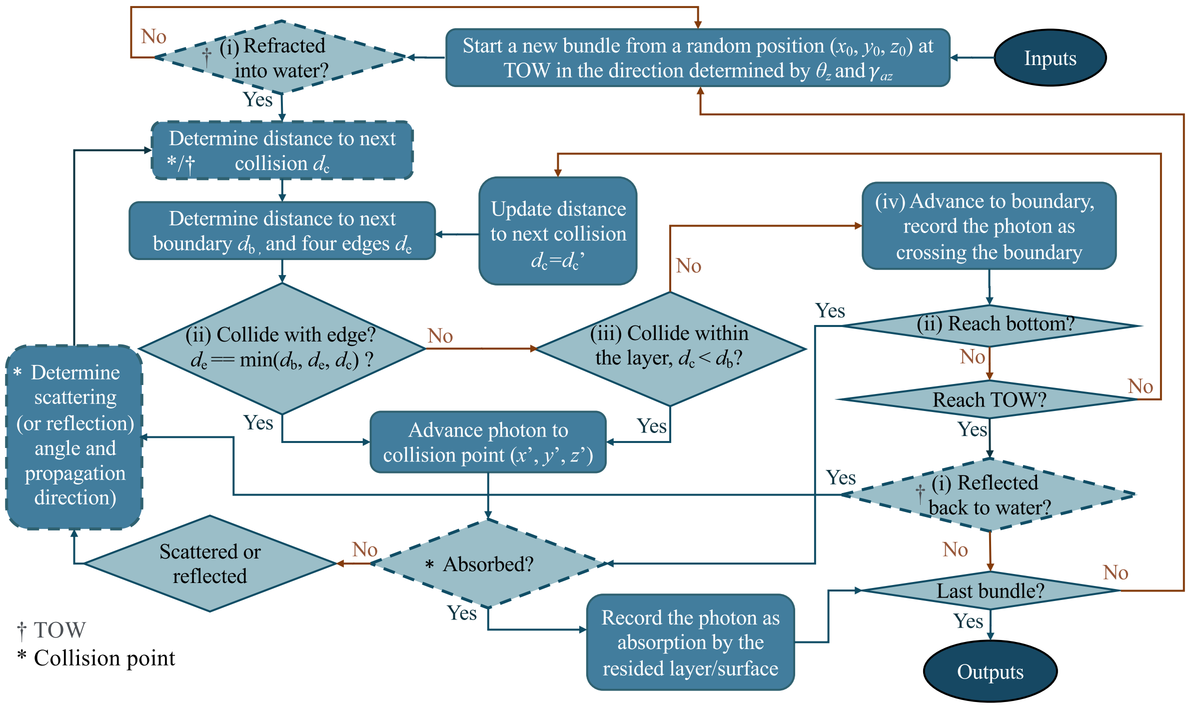


**Fig. 6.** The Monte Carlo process: (i) Photon collision at the air–water interface; (ii) Photon collision at the pond sides or bottom; (iii) Photon interaction with water particles; (iv) Photon travels to the next layer. The processes within the dashed boxes use a random number generator. ∗ and † indicate the random number is generated at the collision point and TOW, respectively.

and $(x', y', z')$ are continually updated until the photon collides with particles, four sides, the bottom, or escapes from the TOW.

### 2.4.3. Photon collision with medium

A photon experiences three types of collisions as depicted in Fig. 6: (i) collision with the air–water interface, resulting in refraction or reflection; (ii) collision with the bottom or the side surfaces, leading to reflection or absorption; and (iii) collision with water particles, leading to absorption or scattering.

(i) Collision with air–water interface: refraction or reflection

At the air–water interface, a photon can undergo refraction or reflection, altering its trajectory according to the Snell law and the Fresnel law (Section 2.3). According to the principle of conservation of energy, the spectral transmittance is $\mathcal{T}_{s,\nu} = 1 - \rho_{s,\nu}$ [29]. In the Monte Carlo simulation, the photon is reflected if the generated $\zeta < \mathcal{T}_{s,\nu}$; otherwise, it undergoes refraction. For photons incident from air to water, reflected photons will be recorded as having left the system. In contrast, for water-to-air incident photons, reflected photons embark on a new journey. Both refraction and reflection are strongly influenced by the angle of incidence and the refractive index of the saline water.

(ii) Collision with bottom or sides: absorption or diffuse reflection

When a photon impinges onto the bottom or one of the four sides of the water pond, it will be reflected or absorbed. All surfaces are considered Lambertian surfaces made of soil. If a generated random number $\zeta < \rho_\nu$, the photon with wavenumber $\nu$ will be reflected, otherwise it will be absorbed. The direction of reflection is sampled by a bunch of new random numbers in the perpendicular plane $\zeta_\perp$ and parallel plane $\gamma_\parallel$ using the expressions $\cos\theta_\perp = \sqrt{\zeta_\perp}$ and $\gamma_\parallel = 2\pi\zeta_\parallel$ [52]. For different collision faces, the expressions corresponding to the $xyz$-axis should be modified according to the right-hand rule for rotation. For example, if a photon is reflected diffusely by the bottom, the updated direction vectors $(r'_x, r'_y, r'_z)$ are:

$$\begin{aligned} r'_z &= \cos\theta_\perp = \sqrt{\zeta_\perp}, \\ r'_x &= \sin\theta_\perp \cos\gamma_\parallel, \\ r'_y &= \sin\theta_\perp \sin\gamma_\parallel. \end{aligned} \tag{7}$$

(iii) Collision with particles: scattering or absorption

When a photon interacts with water particles, it undergoes either absorption or elastic scattering, altering only its direction. If a generated random number $\zeta$ is smaller than the single scattering albedo,

$$\zeta < \rho_\nu = \frac{\kappa_{\mathrm{sca},\nu}}{\kappa_{\mathrm{abs},\nu} + \kappa_{\mathrm{sca},\nu}}, \tag{8}$$

it will be scattered, otherwise it will be counted as absorbed by the water layer. The $\kappa_{\mathrm{sca},\nu}$ and $\kappa_{\mathrm{abs},\nu}$ are the scattering coefficient and the absorption coefficient at the wavenumber $\nu$, respectively. The scattering angle is approximated using the isotropic scattering phase function [52]:

$$P(\cos\Theta) = \frac{1}{4\pi} \tag{9}$$

where $\Theta$ is the angle between the incident direction and the scattering direction.

## 3. Results and discussion

The developed MC-RTM is used to generate results for three research questions, as presented in Table 2: (1) the impact of the directional characteristics of incident radiation on its propagation and absorption in saline water; (2) the impact of spectral characteristics of diffuse radiation on its absorption in saline water; and (3) the relationship between water absorption rate and the depth of the water pond, as well as the nature of incident radiation.

Section 3.1 is designed for applications that employ optical concentrators to enhance the solar radiation received by devices submerged in water. The efficiency of a concentrator in harnessing radiation depends on the angle of incidence. Section 3.2 relates to applications that exploit underwater solar or longwave radiation for processes such as radiation-driven interfacial evaporation, underwater vapor generation, and underwater photovoltaic systems. These applications focus on the spectral distribution of radiation at various depths of saline water body. Section 3.3 offers user-friendly empirical equations for estimating the

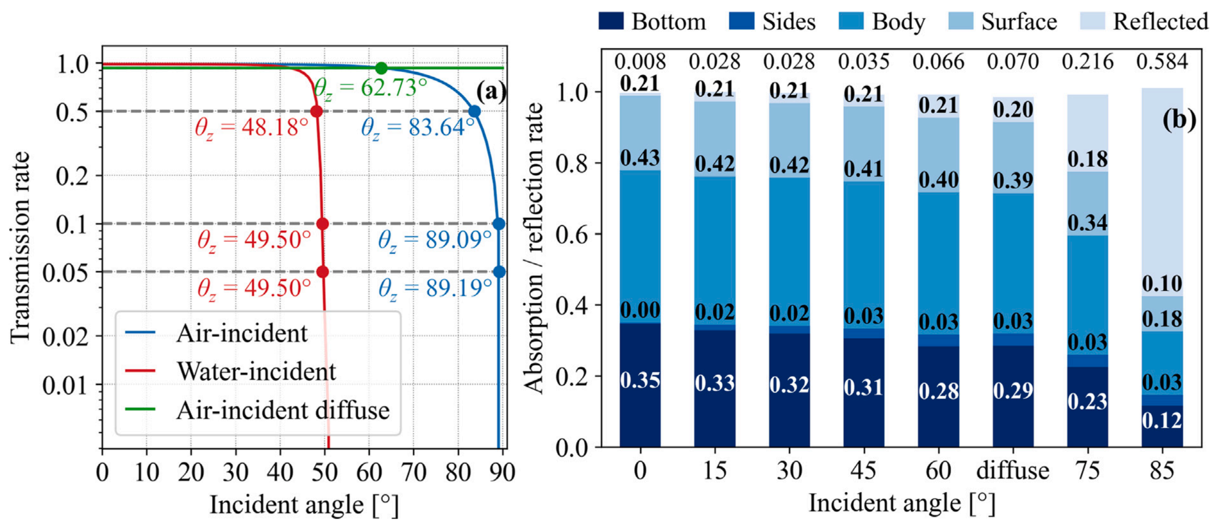


**Fig. 7.** Under solar radiation, the impact of the angle of incidence on water absorptive behavior. (a) Transmission rate of solar radiation on the air–water interface; (b) Effect of incident angle on the absorption and reflection rate distribution. The absorption behavior of diffuse radiation is similar to that of incident radiation at 62.7°.

**Table 2**
Parametric analysis for the three research questions.

| Research question | Angle of incidence | Incident spectrum | Pond depth |
|---|---|---|---|
| Directional characteristics (Section 3.1) | 0–85° and diffuse | Solar spectrum | 2 m |
| Spectral characteristics (Section 3.2) | Diffuse | Solar spectrum 300–5800 K | 2 m |
| Empirical correlation (Section 3.3) | Diffuse | Solar spectrum 1800–5800 K | 0.3–2 m |

absorption of radiation based on the temperature of the blackbody heat source and the depth of the saline water. The water domain analyzed includes the water surface (0 to 1 cm deep), the main saline water body (1 to 199 cm deep), the bottom surface of the pond and four sides, as illustrated in Fig. 1.

### 3.1. Effects of the directional characteristics of incident radiation

This subsection analyzes the impacts of directional characteristics of incident radiation on its propagation, focusing on two primary processes: reflection at the water surface and absorption within the water body. Here, the incident radiation considered only includes solar radiation, since the blackbody emission is often diffused. Using the reflectance data illustrated in Fig. 5, the integrated transmission rate $\mathcal{T}$ is calculated for solar spectra at various angles of incidence. These angles of incidence correspond physically to different solar zenith angles $\theta_z$:

$$\mathcal{T}(\theta_z) = \frac{\int e_{\nu,\text{in}} \cdot \mathcal{T}_\nu(\theta_z)}{\int e_{\nu,\text{in}}} \tag{10}$$

in which $e_{\nu,\text{in}}$ is monochromatic solar flux.

The integrated transmission rate at the water surface is depicted in Fig. 7a. For air-incident radiation, as long as the angle of incidence is less than 62.7°, almost all radiation will transmit into the water without being reflected. For water incident radiation, once the angle of incidence is larger than 49.5°, the radiation will be reflected back into the water. In particular, the transmission rate of diffuse solar radiation is approximately 0.93, which corresponds to the angle of incidence of 62.7° for air-incident beam radiation. This result is in agreement with previous studies [30,32].

In perspective of the absorption within the water body, Fig. 7b shows that once the angle of incidence is less than 62.7°, the absorption rate remains almost the same at water surface, water body and pond sides, since the aspect ratio of the modeled shallow water pond is 10:1 (width to depth), the edges have little impact on water body absorption [45]. However, the increase in the incident angle results in a slightly decrease in the absorption rate at the pond bottom surface. It is because the reflection rate at the air–water interface increased. The water absorption properties of diffuse radiation are similar to that of beam radiation incident from 62.7°, which agrees with Fig. 7a.

### 3.2. Effects of the spectral characteristics of incident radiation

This subsection examines how the spectral characteristics of diffuse radiation affect its absorption in saline water pond. It is analyzed first in terms of the solar spectrum and then in terms of the blackbody emissive spectrum with different heat source temperatures. Fig. 8 depicted the spectral distribution of the absorbed solar flux density in the water pond. The initial 50 cm of water absorbed radiation greater than 1 μm, accounting for about 50% of the energy of incident radiation, while the 50–200 cm depth only absorbs about 10% of incident radiation, mainly the visible band (0.4–0.7 μm) and a part of the near-infrared band (0.7–1 μm). The water surface absorbs all radiation greater than 1.4 μm (20% incident radiation). The first 8 cm depth of the water absorbs all radiation greater than 1.14 μm (more than 30% incident radiation). Most radiation in the visible band is absorbed by the bottom and sides of the water pond. These findings are in agreement with previous studies [55].

Blackbody heat source with different temperatures displays a different spectrum. Analyzing the impacts of the temperature of the heat source will provide more distinctive guidance for industrial applications such as contactless evaporation. Fig. 9 illustrates the distribution of radiation absorption rates in the saline water pond, subjected to radiation from blackbodies with various temperatures. It can be noticed that reflection rates for all temperatures remain around 0.06, and the absorption rate of the water surface keeps at 0.94 before 1300 K, then gradually declines to 0.23 as temperature increases, demonstrating that the water surface can absorb almost all radiation emitted by the blackbody whose temperature is less than 1300 K. Furthermore, the absorption rate within the water body slightly rises from zero to around 0.38 at 4300 K before stabilizing there. The absorption rate of the first 50 cm depth of the water is approximately 0.93 for temperatures below 1300 K, then gradually declines to 0.45 for temperatures of 5800 K.

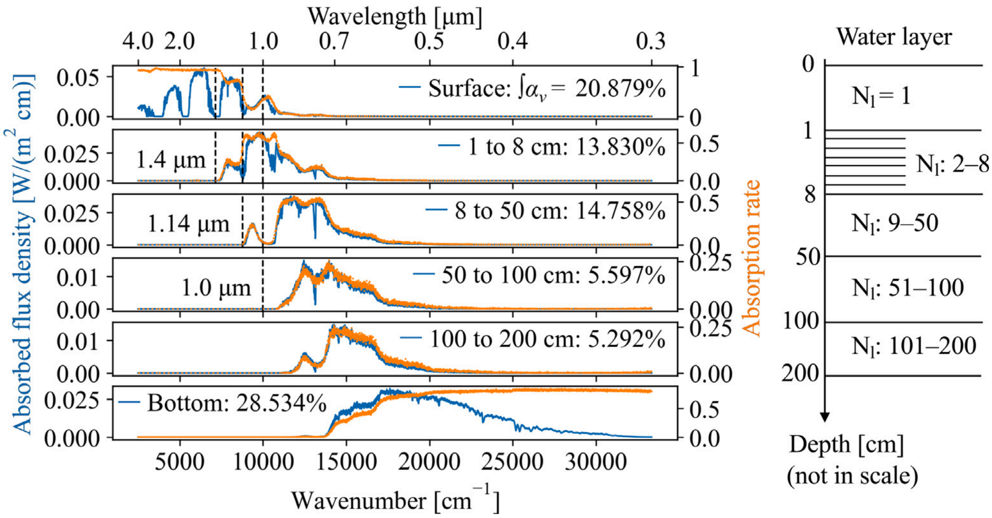


**Fig. 8.** Under diffuse solar radiation, the spectral distribution of absorbed flux density and total absorption rate at various layers of water pond. The first 50 cm depth of water (including the surface) absorbs all radiation greater than 1 μm, accounting for about 50% of incident diffused solar radiation.

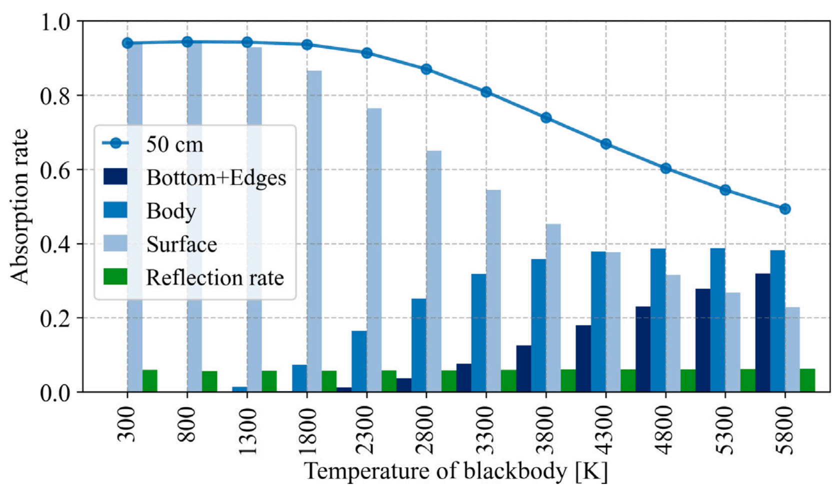


**Fig. 9.** Distribution of radiation absorption rates in the saline water pond exposed to radiation from blackbodies at various temperatures. Almost all radiation emitted by the blackbody $T < 1300$ K is absorbed by the water surface.

### 3.3. Empirical correlations for water absorption rate

This section presents empirical correlations to relate the absorption rate with depth in water and the spectrum of incident radiation, including diffuse solar and blackbody emission. Note that the reflectance of the bottom and sides of the pond is notably low (less than 0.1). Additionally, with an aspect ratio of 10:1, the influence of edge reflection on overall water absorption is minimal [45].

#### 3.3.1. Solar radiation

Under diffuse solar radiation, Fig. 10 illustrates the empirical correlation between the total water absorption rate and the depth of water. Here, the total absorption rate is fitted over two segments of the solar spectrum, with a cutoff at 1 μm. The selection of the cut-off point is based on experimental tests as shown in Fig. 8, with three distinct peaks in the absorption spectrum at 1.4, 1.14, and 1 μm. Here, an ideal cut-off point was determined to be 1 μm. The correlation was evaluated using four types of formulas, denoted by $f_{1,2,3,4}$. Formula $f_1$ is selected because it is based on the Beer's law,

$$\alpha = 1 - e^{-\tau}, \tag{11}$$

in which $\tau$ is the optical depth, equating to the product of the absorption coefficient and the depth of water. The regressed empirical correlations for the two spectral segments are:

$$\begin{aligned} \alpha_{seg1} &= 1 - \exp(-29.2D - 2.38) - 0.74, \quad \lambda > 1\ \mu\text{m} \\ \alpha_{seg2} &= 1 - \exp(-2.25D - 1.29) - 0.67, \quad \lambda \le 1\ \mu\text{m} \end{aligned} \tag{12}$$

in which the water depth $D > 0$. The total absorption rate $\alpha = \alpha_{seg1} + \alpha_{seg2}$.

As illustrated in Fig. 10 a, radiation with wavelengths greater than 1 μm is completely absorbed within the initial 0.5 meters of water depth. The absorption rate is approaching the value of $(1 + C_3)$, which is the fraction of radiation with $\lambda > 1$ μm in the solar spectrum. In contrast, radiation with wavelengths less than 1 μm is not fully absorbed by a water body with a depth of 2 m, as demonstrated in Fig. 10 b. Although the proposed correlation might underestimate the absorption rate for deep water bodies, its accuracy for shallow bodies of water remains well-supported.

#### 3.3.2. Blackbody emissive radiation

Using a similar approach of fitting empirical correlations of solar radiation, a piece-wise function with a cutoff was used to fit the total absorption rate of water under blackbody emission (1300–5800 K). However, unlike the correlations of solar radiation, the regression equations of blackbody emission are divided into three ranges based on

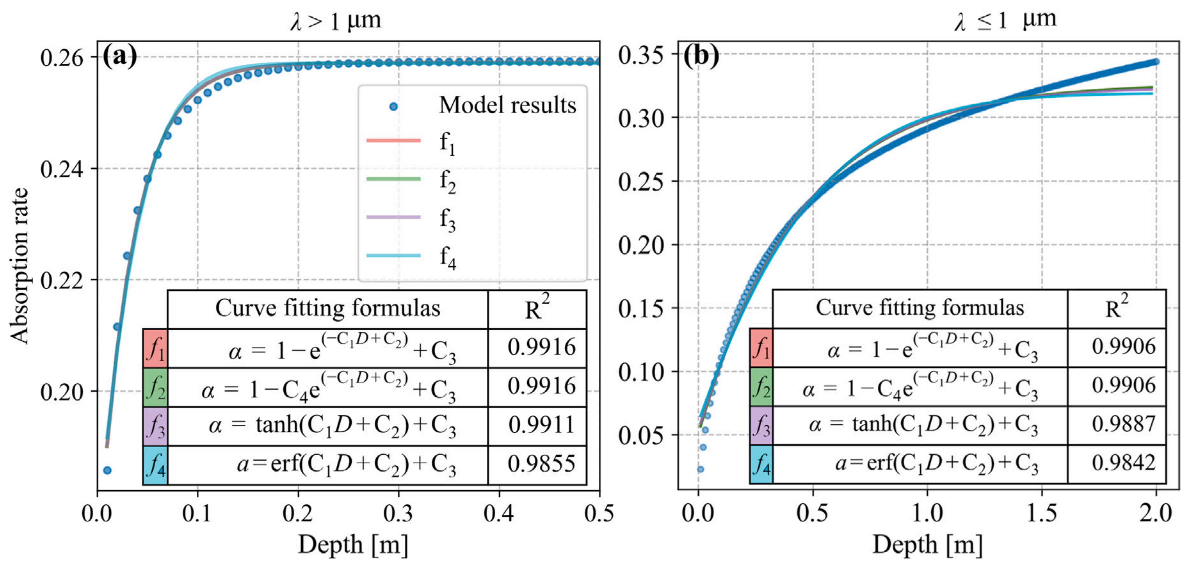


**Fig. 10.** Absorption rate of water under diffuse solar radiation as a function of depth. $\alpha(D) = \alpha_{seg1} + \alpha_{seg2}$.

**Table 3**
Empirical correlations of absorption rate with respect to water depth and the temperature of blackbody heat source.

| Temperature [K] | Band [μm] | Correlations ($\alpha = \alpha_{seg1} + \alpha_{seg2}$) | Correlations coefficients $C_{1,2,3}$ as the function of $T' = T/1000$ |
|---|---|---|---|
| $T \leq 1300$ | 0.25–4 | 0.93, Fig. 9 | – |
| $1400 \leq T < 2300$ | $\lambda > 1.14$ | $\alpha_{seg1} = 1 - e^{(-C_1 \cdot D + C_2)} + C_3$ Fig. 11a | $C_1 = 496.32T'^2 - 265.56T' + 41.61$ $C_2 = -159.1T'^2 + 81.47T' - 12.56$ $C_3 = 6.64T'^2 - 0.88T' - 0.99$ Fig. 12a–c |
| | $\lambda \leq 1.14$ | $\alpha_{seg2} = 1 - e^{(-C_1 \cdot D + C_2)} + C_3$ Fig. 11b | $C_1 = 1749.64T'^2 - 830.9T' + 107.06$ $C_2 = -117.76T'^2 + 61.52T' - 10$ $C_3 = 2.99T'^2 + 1.45T' - 1.21$, Fig. 12d–f |
| $2300 \leq T \leq 5800$ | $\lambda > 1$ | $\alpha_{seg1} = 1 - e^{(-C_1 \cdot D + C_2)} + C_3$ Fig. 13a | $C_1 = 49.25T'^2 - 54.11T' + 45.64$ $C_2 = -8.82T'^2 + 6.22T' - 3.18$ $C_3 = 2.24T'^2 - 3.43T' + 0.5$ Fig. 14a–c |
| | $\lambda \leq 1$ | $\alpha_{seg2} = 1 - e^{(-C_1 \cdot D + C_2)} + C_3$ Fig. 13b | $C_1 = 13.31T'^2 - 16.69T' + 7.15$ $C_2 = -16.41T'^2 + 16.68T' - 5.52$ $C_3 = -2.45T'^2 + 2.62T' - 1.37$ Fig. 14d–f |

temperature, as shown in Table 3. The reasons for the division are: (i) Blackbody emission of $T \leq 1300$ K is fully absorbed by the first 1 cm of water body, as shown in Fig. 9; (ii) Blackbody emission from heat sources of 1300 K < $T$ < 2300 K can penetrate the first 1 cm depth of the water and 1.14 μm is determined as the cut-off point as indicated in Fig. 8. (iii) The fitting processing for blackbody emission of 2300–5800 K is the same as that of solar radiation with 1 μm as the cut-off point.

Figs. 11 and 13 illustrate the fitting results of absorption rate with blackbody heat source of 1400 K ≤ $T$ < 2300 K and 2300 K < $T$ < 5800 K, respectively. The Mean Absolute Percentage Error (MAPE), Root Mean Squared Error (RMSE), and $R^2$ are used to evaluate the accuracy of the regression, as shown in Figs. 11 and 13. The regression coefficients have been found to vary as a function of the heat source temperature. To facilitate simpler computations across a broad spectrum of heat source temperatures, these coefficients have been modeled using a quadratic function, as shown in Figs. 12 and 14.

### 3.4. Discussion

This work used an MC-RTM to investigate the effects of the spectral and directional properties of incident radiation on its propagation at various water depths:

- The analysis of directional characteristics indicates that if the incident angle of solar radiation is less than 62.7°, the angle has a negligible impact on the absorption rates of both the water surface and the water body. This finding could be applied to the design of more efficient solar concentrators.
- The spectral characteristic analysis shows that radiation with wavelengths longer than 1.4 μm, 1.14 μm, 1 μm is completely absorbed within the first 1, 8 and 50 cm of the water, respectively. For contactless interfacial evaporation applications, it is recommended to consider utilizing a heat source spectrum predominantly above 1.4 μm. Furthermore, it may be beneficial to maintain the temperature of the emitting heat source at or below 1300 K to maximize interfacial absorption of incident radiation.
- Empirical correlations have been developed to facilitate the estimation of absorption rates at varying water depths. These correlations can be used effectively to determine the optimal depth for applications such as underwater vapor generation and submerged photovoltaic systems.

Note that the empirical formula derived in this work is based on saline water with a fixed temperature of 20 °C and a salinity of 35 ppt. In conditions of lower salinity or higher temperature, the absorption rate will be slightly higher, and conversely, in environments with

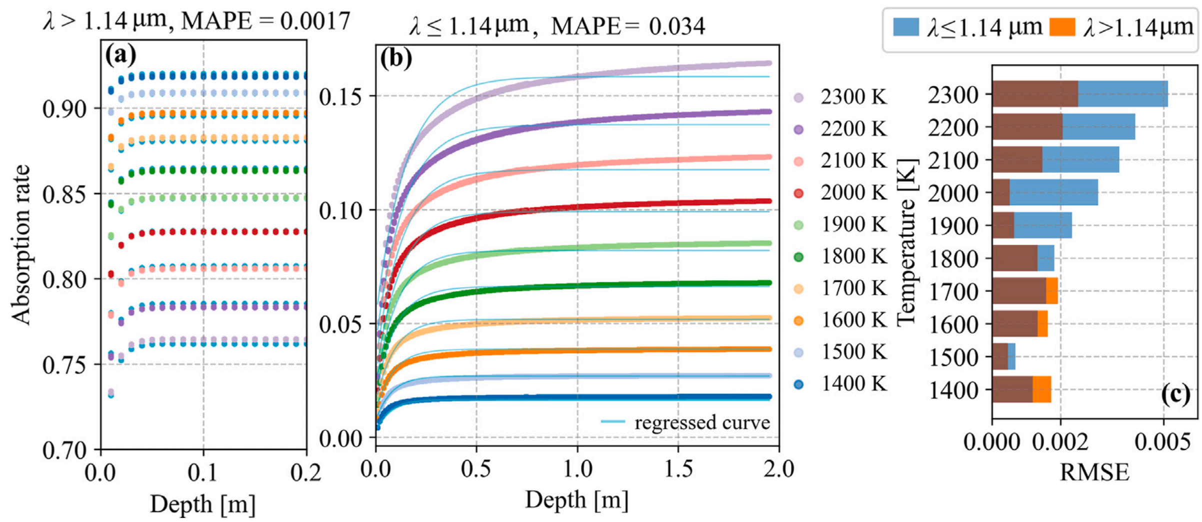


**Fig. 11.** Absorption rate as a function of water depth and the temperature of blackbody heat source when 1400 K $\leq T <$ 2300 K ; (a) $\lambda >$ 1.14 µm. (b) $\lambda \leq$ 1.14 µm. The pale blue curve indicates the regressed correlations. (c) The RMSE of fitted result of each temperature.

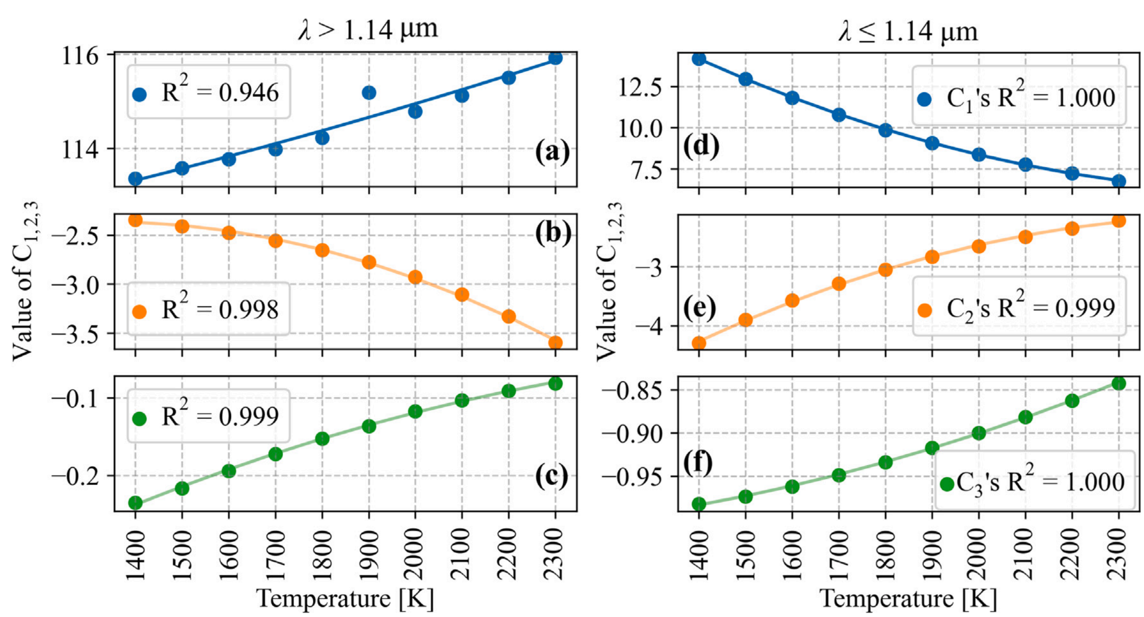


**Fig. 12.** The $R^2$ for regression coefficients as a function of heat source temperature. (a,b,c) $R^2$ when $\lambda >$ 1.14 µm corresponding to Fig. 11a ; (d,e,f) $R^2$ when $\lambda \leq$ 1.14 µm corresponding to Fig. 11b.

higher salinity or lower temperature, the absorption rate will be slightly lower [29]. Furthermore, the MC-RTM model does not account for polarization and photomolecular effects [56,57]. Polarization may cause slight deviations in the trajectory of photons, whereas photomolecular interactions can enable a photon in the green spectrum to transition liquid water directly to the vapor phase, potentially enhancing evaporation rates. Furthermore, the model is limited to saline water as the medium of study. Future research should consider incorporating a broader range of mediums, such as nanofluids and colored dissolved organic matter, to extend the applicability of the model to a wider array of aquatic environments.

## 4. Conclusions

Comprehensive knowledge of how radiation propagates in saline water considering its spectral and directional characteristics provides guidance for applications such as radiative evaporation at the air–water interface, underwater vapor generation and underwater photovoltaic systems. In this work, a Monte Carlo radiative transfer model is developed considering the full complexity of the spectral and angular dependence of the radiation to simulate the transfer of radiation in a saline water pond. The incident radiation includes not only diffuse and beam solar radiation, but also diffuse blackbody (300–5800 K) emissive radiation.

For directional characteristics, the effect of diffuse radiation is comparable to beam radiation at about 62.7°. In addition, the incident angle has little impact on the absorption rate of the water surface and water body if the incident angle is less than 62.7°. For spectral characteristics, radiation with wavelength less than 1.4 µm, 1.14 µm and 1 µm are completely absorbed by the first 1 cm, 8 cm and 50 cm depth of the water layers, accounting for 20%, 30% and 50% of incident diffuse

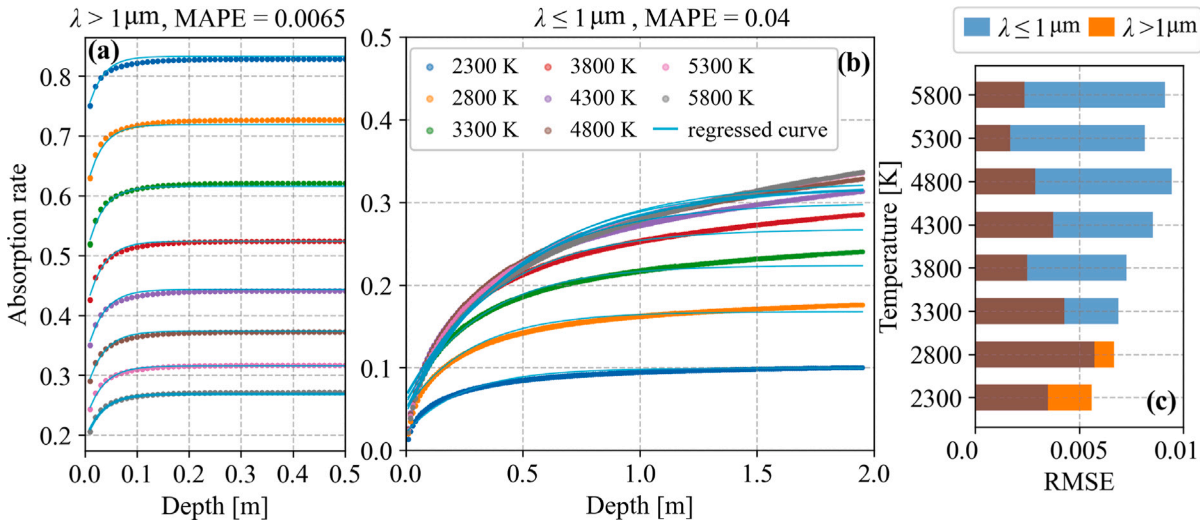


**Fig. 13.** Absorption rate as a function of water depth and the temperature of blackbody heat source when 2300 K < $T$ < 5800 K ; (a) $\lambda > 1$ μm. (b) $\lambda \leq 1$ μm.

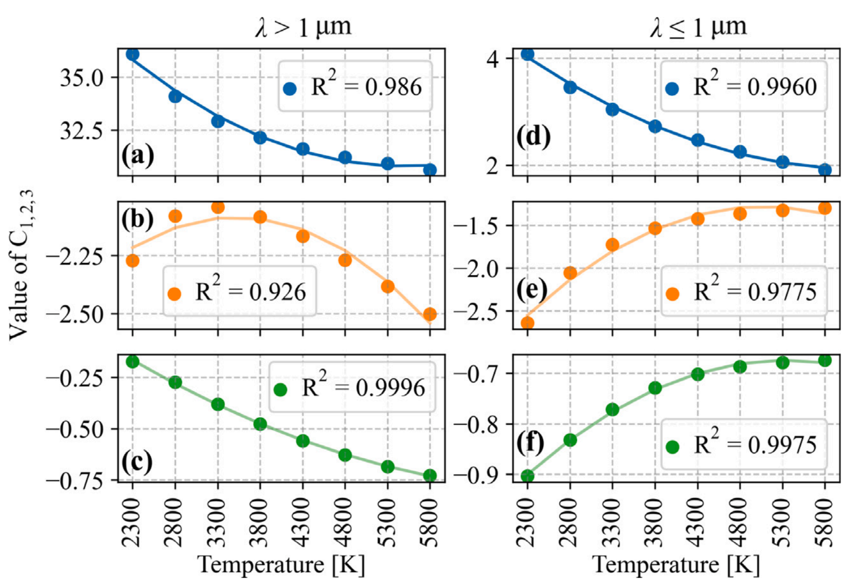


**Fig. 14.** The $R^2$ for regression coefficients as a function of heat source temperature. (a,b,c) corresponds to Fig. 13a when $\lambda > 1$ μm ; (d,e,f) corresponds to Fig. 13b when $\lambda \leq 1$ μm.

solar radiation. Moreover, empirical correlations have been established to enable more straightforward calculations of the water absorption rate at varying depths and for different types of incident radiation. These results will serve as valuable tools for efficiently estimating how radiation propagates through a body of saline water. They will provide data and insights that guide the selection of spectrum-shifting materials and the strategic placement of underwater absorbers/devices for a range of applications in the energy-water nexus.

However, the current model has certain limitations, such as its exclusion of polarization and photomolecular effects, and its applicability only to homogeneous saline water as the study medium. To improve the robustness and applicability of the model, future work will explore a broader range of medium, including nanofluids and colored dissolved organic matter, and will also consider the effects of medium inhomogeneity. Additionally, integrating the MC-RTM code with other energy-related processes, such as natural convection, could address more complex research questions and significantly expand the scope of use of the model in diverse aquatic environments.

## Declaration of competing interest

The authors declare that they have no known competing financial interests or personal relationships that could have appeared to influence the work reported in this paper.

## Data availability

Data will be made available on request.

## Declaration of Generative AI and AI-assisted technologies in the writing process

During the preparation of this work, the authors used GPT-4 in order to improve the language. After using this tool/service, the authors reviewed and edited the content as needed and take full responsibility for the content of the publication.

## Acknowledgments

This work is substantially supported by two grants from the Research Grants Council of the Hong Kong Special Administrative Region, China (Project No. 25213022 and C6003-22Y). The authors express their gratitude to Dr. Lu Wang for providing insightful comments that improved the manuscript.

## Appendix

### *Grid convergence test*

Grid convergence tests are conducted to determine the optimal number of photon bundles $N_b$ per wavelength, as well as the required spectral resolution $\Delta\nu$, to balance accuracy and computational efficiency. The depth of water layers $\Delta l$ was established at 1 cm to facilitate the analysis of water absorption behavior with a vertical resolution of 1 cm. The parameters for these independent tests are detailed in Table A.1.

The model parameters are determined by calculating the convergence rate $r_c$,

$$r_c = \left(1 - \frac{|y_i - y_a|}{y_a}\right) \times 100\%, \tag{13}$$

where $y_i$ represents the result of the current test, while $y_a$ corresponds to the result of the most accurate test, which is computed when the spectral resolution $\Delta\nu$ is set to 1 cm$^{-1}$ and the number of photon bundles $N_b$ equals 5000. A value of $r_c$ that approaches 100% indicates a higher accuracy of the $i$th test. The simulations were executed on an Intel i9-13900K with 32 cores, utilizing Python's multi-processing capabilities for parallel execution. As indicated in Fig. A.1, the optimal spectral resolution, $\Delta\nu$, for both solar and blackbody spectrum is 5 cm$^{-1}$. This resolution achieves an $r_c$ exceeding 99.99%, while doubling the computational speed compared to a resolution of 3 cm$^{-1}$. The ideal number of photon bundles, $N_b$, is identified as 1000. This quantity delivers performance nearly identical to that of 5000 bundles ($r_c$ = 99%) but requires only a fifth of the computational time.

In sum, the model resolution and grid settings are $N_b = 1000$, $\Delta\nu = 5$ cm$^{-1}$, and $\Delta l = 1$ cm for all the cases examined in this work.

### *Model validation*

The Monte Carlo model presented in this work is validated against the mathematical formulation developed by Cengel and Özişik [30] and the Ansys Zemax commercial software. The case considered by Cengel and Özişik [30] involves a one-dimensional pure water pond with a depth of 2 m. Their assumptions include: (i) a constant reflectivity at the air–water interface of 0.066 for the air side and 0.477 for the water side, (ii) no scattering, and (iii) a pond bottom albedo of 0.3. Fig. A.2a shows that the results of the developed MC-RTM are consistent with those of Cengel and Özişik [30], achieving a RMSE of less than 0.05. The MC-RTM results indicate higher absorption at the bottom and lower absorption within the water body. This difference arises because the reference formulation assumes that all radiation reflected back to the water body at the water-air interface is absorbed by the water body without reaching the pond bottom again. In contrast, the MC-RTM provides a more accurate representation by effectively tracking multiple reflections between the bottom of the pond and the water-air interface.

To validate the model against Zemax, Fig. A.2b presents a comparison of the transmission of monochromatic radiation in a 2-meter-deep saline water pond, using data generated by MC-RTM and Zemax simulations. Five wavelengths are considered: infrared (1.5 μm), red (0.75 μm), green (0.5 μm), blue (0.46 μm), and UV (0.35 μm). The results from the MC-RTM simulations are consistent with those from Zemax, exhibiting an average RMSE of less than 0.01.

**Table A.1**
Settings for independent test parameters.

| Model setting | Incident radiation | Saline water pond |
|---|---|---|
| $\Delta\nu$ = 1, 3, 5[a], 10 | Solar spectrum/blackbody $T$ = 5800 K | $L$ = 10 m, $W$ = 10 m, $D$ = 2 m |
| $N_b$ = 100, 500, 1000[a], 5000 | Angle of incidence = 0° | $T$ = 20 °C |
| $\Delta l$ = 1 cm | Randomly distributed incident location | $S$ = 35 ppt |

[a] Denotes parameters determined in accordance with the grid convergence test results.

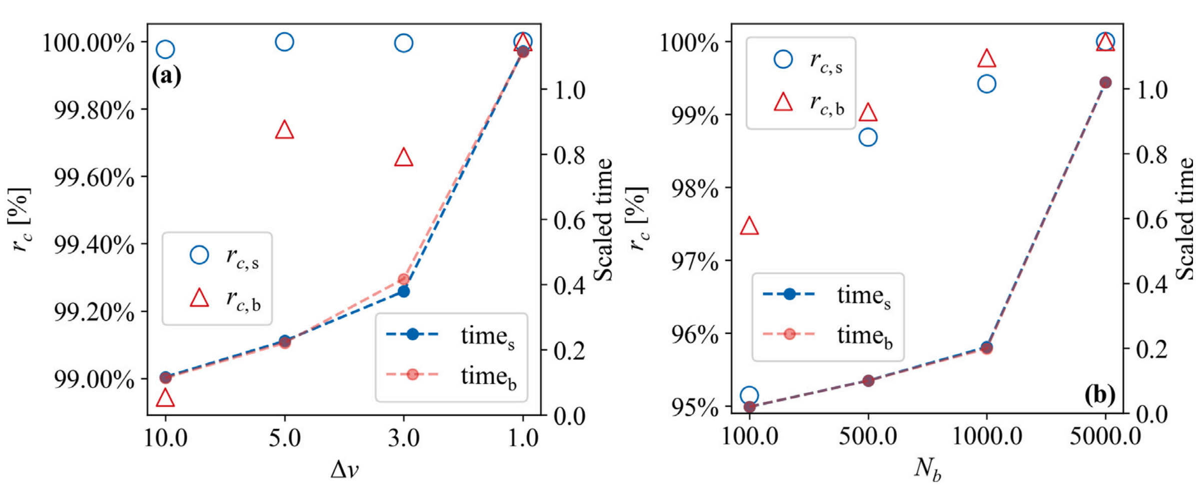


**Fig. A.1.** Grid convergence test for (a) Spectral Resolution, and (b) Bundle Quantity. The symbols $s$ and $b$ represent solar and blackbody emissive radiation, respectively. The grid convergence rate $r_c$ achieving 99% is the baseline for grid convergence.

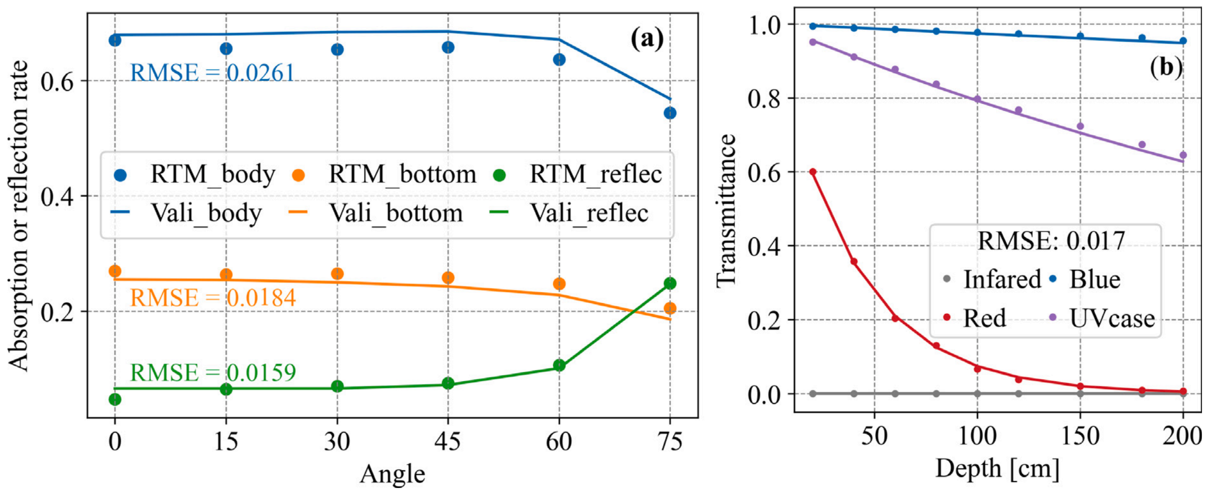


**Fig. A.2.** Validation of the MC-RTM Model. (a) Comparison with theoretical results from Cengel and Özişik [30] on the propagation of solar radiation in a pure water pond. (b) Comparison with Zemax for the propagation of five monochromatic radiation in a saline water pond. The RMSEs for both validation cases are below 0.05.

## References


[1] G.E. Thomas, K. Stamnes, Radiative Transfer in the Atmosphere and Ocean, Cambridge University Press, 2002.

[2] S. Lv, J. Ren, Q. Zhang, B. Zhang, Y. Lai, J. Yang, Z. Chang, Z. Zhan, Design, fabrication and performance analysis of a cost-effective photovoltaic interface seawater desalination hybrid system for co-production of electricity and potable water, Appl. Energy 336 (2023) 120811.

[3] A. Baghizade, F. Farahbod, O. Alizadeh, Laboratory and mathematical investigation of salt deposition in a closed solar desalination pond, Environ. Dev. Sustain. (2023) 1–13.

[4] I.A. Said, N. Fuentes, Z. He, R. Xin, K. Zuo, W.S. Walker, Q. Li, Treatment of brackish water reverse osmosis brine using only solar energy, Environ. Sci.: Water Res. Technol. 7 (10) (2021) 1840–1851.

[5] J. Lan, W. Hong, Y. Chang, C. Dong, H. Li, Manipulating wicking for achieving water-heat-vapor-salt balance in a two-dimensional solar evaporator, Appl. Therm. Eng. 240 (2024) 122234.

[6] S. Jing, Q. Ji, A. Wang, J. Zhao, H. Liang, F. Chen, P. Kannan, P. Tsiakaras, Fe-based metal organic frameworks decorated wood for efficient solar-driven interfacial water evaporation, Appl. Therm. Eng. 244 (2024) 122629.

[7] Q. Zhang, X. Sun, Y. Shen, Y. Zhang, Q. Cai, W. Deng, S. Rao, X. Wu, Q. Ye, Establishing a transient model of double-layer porous media interfacial evaporation system to reveal the relationship between porous media parameters and evaporation performance, Appl. Therm. Eng. 234 (2023) 121311.

[8] A.K. Menon, I. Haechler, S. Kaur, S. Lubner, R.S. Prasher, Enhanced solar evaporation using a photo-thermal umbrella for wastewater management, Nat. Sustain. 3 (2) (2020) 144–151.

[9] O.K. Varghese, M. Paulose, T.J. LaTempa, C.A. Grimes, High-rate solar photocatalytic conversion of $CO_2$ and water vapor to hydrocarbon fuels, Nano Lett. 9 (2) (2009) 731–737.

[10] H. Nisar, A.K. Janjua, H. Hafeez, N. Shahzad, A. Waqas, et al., Thermal and electrical performance of solar floating PV system compared to on-ground PV system-an experimental investigation, Sol. Energy 241 (2022) 231–247.

[11] M.R. Clot, P. Rosa-Clot, G.M. Tina, Submerged PV solar panel for swimming pools: SP3, Energy Procedia 134 (2017) 567–576, Sustainability in Energy and Buildings 2017: Proceedings of the Ninth KES International Conference, Chania, Greece, 5-7 July 2017.

[12] P. Tao, G. Ni, C. Song, W. Shang, J. Wu, J. Zhu, G. Chen, T. Deng, Solar-driven interfacial evaporation, Nat. Energy 3 (12) (2018) 1031–1041.

[13] F. Cao, K. McEnaney, G. Chen, Z. Ren, A review of cermet-based spectrally selective solar absorbers, Energy Environ. Sci. 7 (5) (2014) 1615–1627.

[14] M. Gao, L. Zhu, C.K. Peh, G.W. Ho, Solar absorber material and system designs for photothermal water vaporization towards clean water and energy production, Energy Environ. Sci. 12 (3) (2019) 841–864.

[15] T.A. Cooper, S.H. Zandavi, G.W. Ni, Y. Tsurimaki, Y. Huang, S.V. Boriskina, G. Chen, Contactless steam generation and superheating under one sun illumination, Nat. Commun. 9 (1) (2018) 5086.

[16] O. Neumann, A.S. Urban, J. Day, S. Lal, P. Nordlander, N.J. Halas, Solar vapor generation enabled by nanoparticles, ACS Nano 7 (1) (2013) 42–49.

[17] P. Wang, Emerging investigator series: the rise of nano-enabled photothermal materials for water evaporation and clean water production by sunlight, Environ. Sci.: Nano 5 (5) (2018) 1078–1089.

[18] P. Godart, Design and simulation of a heat-driven direct reverse osmosis device for seawater desalination powered by solar thermal energy, Appl. Energy 284 (2021) 116039.

[19] Q.R. Al-Amir, H.K. Hamzah, F.H. Ali, M. Hatami, W. Al-Kouz, A. Al-Manea, R. Al-Rbaihat, A. Alahmer, Investigation of natural convection and entropy generation in a porous titled Z-staggered cavity saturated by TiO2-water nanofluid, Int. J. Thermofluids 19 (2023) 100395.

[20] Z. Al-Dulaimi, H.T. Kadhim, M.F. Jaffer, A. Al-Manea, R. Al-Rbaihat, A. Alahmer, Enhanced conjugate natural convection in a corrugated porous enclosure with ag-mgo hybrid nanofluid, Int. J. Thermofluids 21 (2024) 100574.

[21] P.K. Enaganti, P.K. Dwivedi, R. Sudha, A.K. Srivastava, S. Goel, Underwater characterization and monitoring of amorphous and monocrystalline solar cells in diverse water settings, IEEE Sens. J. 20 (5) (2020) 2730–2737.

[22] J.A. Röhr, B.E. Sartor, J.N. Duenow, Z. Qin, J. Meng, J. Lipton, S.A. Maclean, U. Römer, M.P. Nielsen, S. Zhao, et al., Identifying optimal photovoltaic technologies for underwater applications, Iscience 25 (7) (2022).

[23] J.A. Röhr, B.E. Sartor, J. Lipton, A.D. Taylor, A dive into underwater solar cells, Nat. Photonics 17 (9) (2023) 747–754.

[24] H. Ghasemi, G. Ni, A.M. Marconnet, J. Loomis, S. Yerci, N. Miljkovic, G. Chen, Solar steam generation by heat localization, Nat. Commun. 5 (1) (2014) 4449.

[25] G. Ni, G. Li, S.V. Boriskina, H. Li, W. Yang, T. Zhang, G. Chen, Steam generation under one sun enabled by a floating structure with thermal concentration, Nat. Energy 1 (9) (2016) 1–7.

[26] G. Kuznetsov, M. Piskunov, R. Volkov, P. Strizhak, Unsteady temperature fields of evaporating water droplets exposed to conductive, convective and radiative heating, Appl. Therm. Eng. 131 (2018) 340–355.

[27] R. Viskanta, J. Toor, Absorption of solar radiation in ponds, Sol. Energy 21 (1) (1978) 17–25.

[28] A. Abbassi Monjezi, A. Campbell, A comprehensive transient model for the prediction of the temperature distribution in a solar pond under mediterranean conditions, Sol. Energy 135 (2016-10) 297–307.

[29] C. Mobley, The oceanic optics book, 2022, Available at https://www.oceanopticsbook.info (2023/05/20).

[30] Y. Cengel, M. Özişik, Solar radiation absorption in solar ponds, Sol. Energy 33 (6) (1984) 581–591.

[31] M. Husain, S. Patil, P. Patil, S. Samdarshi, Simple methods for estimation of radiation flux in solar ponds, Energy Convers. Manage. 45 (2) (2004) 303–314.

[32] H. Wu, R. Tang, Z. Li, H. Zhong, A mathematical procedure to estimate solar absorptance of shallow water ponds, Energy Convers. Manage. 50 (7) (2009) 1828–1833.

[33] A.M. Daabo, E. Bellos, S. Pavlovic, M.A. Bashir, S. Mahmoud, R.K. Al-Dadah, Characterization of a micro thermal cavity receiver–experimental and analytical investigation, Therm. Sci. Eng. Prog. 18 (2020) 100554.

[34] A.M. Daabo, Y.S. Al-Mola, A.Y. Al-Rawy, T. Lattimore, State of the art single-objective optimization of small scale cylindrical cavity receiver, Sustain. Energy Technol. Assess. 35 (2019) 278–290.

[35] D. Freier, F. Muhammad-Sukki, S.H. Abu-Bakar, R. Ramirez-Iniguez, A.A. Mas'ud, R. Albarracín, J.A. Ardila-Rey, A.B. Munir, S.H.M. Yasin, N.A. Bani, Software simulation and experimental characterisation of a rotationally asymmetrical concentrator under direct and diffuse solar radiation, Energy Convers. Manage. 122 (2016) 223–238.

[36] C.D. Mobley, E.S. Boss, Improved irradiances for use in ocean heating, primary production, and photo-oxidation calculations, Appl. Opt. 51 (27) (2012) 6549–6560.

[37] L. Ma, F. Wang, C. Wang, C. Wang, J. Tan, Monte Carlo simulation of spectral reflectance and BRDF of the bubble layer in the upper ocean, Opt. Express 23 (19) (2015) 24274–24289.

[38] J. Tan, Y. Xie, F. Wang, L. Jing, L. Ma, Investigation of optical properties and radiative transfer of TiO2 nanofluids with the consideration of scattering effects, Int. J. Heat Mass Transfer 115 (2017) 1103–1112.

[39] L. Wang, Y. Feng, Q. Liu, G. Liu, Solar-thermo-radiative evaporator for continuous steam generation and salt harvesting, Sol. Energy 250 (2023) 347–354.

[40] H. Liang, F. Wang, L. Yang, Z. Cheng, Y. Shuai, H. Tan, Progress in full spectrum solar energy utilization by spectral beam splitting hybrid PV/T system, Renew. Sustain. Energy Rev. 141 (2021) 110785.

[41] H. Wu, S. Shan, J. Tian, G. Zhang, Z. Zhou, Thermodynamic theorical and parametric analysis of a photovoltaic-photo/thermochemistry synergistic conversion system with full spectrum cascading utilization, Energy Convers. Manage. 314 (2024) 118701.

[42] C.D. Mobley, Light and Water: Radiative Transfer in Natural Waters, Academic Press, 1994.

[43] S.K. Meerdink, S.J. Hook, D.A. Roberts, E.A. Abbott, The ECOSTRESS spectral library version 1.0, Remote Sens. Environ. 230 (2019) 111196, URL https://speclib.jpl.nasa.gov.

[44] A.M. Baldridge, S.J. Hook, C. Grove, G. Rivera, The ASTER spectral library version 2.0, Remote Sens. Environ. 113 (4) (2009) 711–715.

[45] J. Hull, K. Liu, W. Sha, J. Kamal, C. Nielsen, Dependence of ground heat loss upon solar pond size and perimeter insulation calculated and experimental results, Sol. Energy 33 (1) (1984) 25–33.

[46] Y. Zhang, X. Ge, Y. Li, C. Li, Mathematical simulation of evaporating brine by solar radiation for the production of salt, J. Therm. Sci. 2 (1993) 143–151.

[47] R. Röttgers, R. Doerffer, D. McKee, W. Schönfeld, Pure Water Spectral Absorption, Scattering, and Real Part of Refractive Index Model Algorithm Technical Basis Document, Univ. Strat. Glas, 2010, pp. 1–18.

[48] X. Zhang, L. Hu, M.-X. He, Scattering by pure seawater: Effect of salinity, Opt. Express 17 (7) (2009) 5698–5710.

[49] T.A.S. for Testing, Materials, Reference solar spectral irradiance: ASTM G-173, 2004, Available at https://www.nrel.gov/grid/solar-resource/spectra-am1.5.html (2023/05/20).

[50] A.F. Mills, C.F.M. Coimbra, Basic Heat and Mass Transfer Temporal Publishing, LLC, 2015.

[51] M. Li, Z. Liao, C.F.M. Coimbra, Spectral model for clear sky atmospheric longwave radiation, J. Quant. Spectrosc. Radiat. Transfer 209 (2018) 196–211.

[52] M. Li, Z. Liao, C.F.M. Coimbra, Spectral solar irradiance on inclined surfaces: A fast Monte Carlo approach, J. Renew. Sustain. Energy 12 (5) (2020) 053705.

[53] P. Yang, C. van der Tol, T. Yin, W. Verhoef, The SPART model: A soil-plant-atmosphere radiative transfer model for satellite measurements in the solar spectrum, Remote Sens. Environ. 247 (2020) 111870.

[54] K.L. Coulson, Polarization and Intensity of Light in the Atmosphere, A Deepak Pub, 1988.

[55] C. Valderrama, J. Luis Cortina, A. Akbarzadeh, Chapter 14 - Solar Ponds, in: T.M. Letcher (Ed.), Storing Energy, Elsevier, Oxford, 2016, pp. 273–289.

[56] G. Lv, Y. Tu, J.H. Zhang, G. Chen, Photomolecular effect: Visible light interaction with air–water interface, Proc. Natl. Acad. Sci. 121 (18) (2024) e2320844121.

[57] L.X. Dang, T.-M. Chang, Molecular dynamics study of water clusters, liquid, and liquid–vapor interface of water with many-body potentials, J. Chem. Phys. 106 (19) (1997) 8149–8159.